EI SEVIER

Contents lists available at ScienceDirect

Powder Technology

journal homepage: www.elsevier.com/locate/powtec



Smoothed particle hydrodynamics simulation of granular system under cyclic compressions



Raihan Tayeb ¹, Yijin Mao ², Yuwen Zhang *

Department of Mechanical and Aerospace Engineering, University of Missouri, Columbia, MO 65211, USA

ARTICLE INFO

Article history:
Received 4 December 2018
Received in revised form 4 April 2019
Accepted 28 April 2019
Available online 11 May 2019

Keywords:
Smooth particle hydrodynamics
Jamming
Granular material
Contact model
Force chain

ABSTRACT

The response of two-dimensional frictionless granular material to isotropic cyclic compression is simulated using an improved version of the Smoothed Particle Hydrodynamics (SPH) method, which includes realistic constitutive model for deformation of individual grains. The study reveals the evolution of mean coordination number and global pressure over cycles. The probability distribution function (PDF) of contact forces for different compression cycles is also reported. The global pressure at maximum compression shows downward trend for packing fractions below a certain value. The structural rearrangement that can give rise to such stress relaxation is studied by mapping relative particle mobilities and quantifying dynamic heterogeneity using a four-point susceptibility measure. The four-point susceptibility measure reveals length and time scales that can characterize the dynamics of driven system. Meso-scale structural rearrangement is studied using Falk-Langer measure of affine and non-affine deformation. The affine and non-affine deformations drop to a stable value and oscillates around it, which suggest that the structure is driving towards a more stable configuration. A negative correlation is found between the local packing fraction and the non-affine squared displacement. Finally, a complex network analysis is employed to better understand the structural rearrangement at meso-scale. The average degree and average clustering coefficient obtained from the complex network analysis show peaks at maximum compressions, but the peak values increase with cycles. The degree per particle is found to be positively correlated with local packing fraction and negatively correlated with the non-affine squared deformation. An enrichment of three-cycle population is seen, suggesting it as the most preferred conformation for particles at the meso-scale. © 2019 Elsevier B.V. All rights reserved.

1. Introduction

Granular materials, such as sand, are collection of discrete macroscopic particles which exhibit a wide range of interesting macroscopic behaviors such as pile formation, fluid-flow like behavior, and fracture. They are important in many industrial applications such as mining, construction, agriculture, and packing. They also play an important role in geological processes such as landslide, avalanche, erosion, sedimentation, and plate tectonics. One particular aspect of granular material is the phenomenon of jamming where randomly organized system of particles changes from mechanically unstable states to stable states. Jamming phenomena are also observed in colloids, foams, and glass transition in molecular liquids. In most of these cases, the system starts from an unjammed state and gradually transition to a jammed state. Sometimes the system undergoes several transitions between jammed and unjammed states. By careful micromechanical simulations like the

* Corresponding author.

one presented here, one can study the jamming behavior of the system under different loading conditions and derive macroscopic model to replicate such behavior.

Simulations of granular materials in the past have revealed important aspects in the dynamics of jamming of granular materials. For example, Thornton [1] and Suiker et al. [2] studied the stress-strain response of using Discrete Element Method (DEM). Jia et al. also used DEM to study effect of particle size and size distribution [3–5]. Tayeb et al. provided extensive data on the effect of cohesion and van der Waals using a history dependent contact force model [6]. All these models have their own ways of idealizing the material properties of granular particles and their interactions, such as assuming all particles as viscoelastic or using a linear spring to model contact force, etc. However, one can make use of the constitutive models that are available for each individual particle for simulating real granular materials. A computational method that can provide such convenience and at the same time allows easy extension to irregular shaped particles is always a lucrative option for researchers in granular physics.

In this paper the jammed states of two dimensional granular materials is numerically investigated by subjecting the system to consecutive compression cycles. The dynamics of near jammed isotropically driven

E-mail address: zhangyu@missouri.edu (Y. Zhang).

¹ Both authors contributed equally to this work.

² Current address: Shenzhen Escope Technology Co.Ltd., Shenzhen 518,052, China.

Table 1Material properties.

	ρ (g/cm ³)	c (×10 ⁴ m/s)	S	G (GPa)	E (GPa)	Γ
Lead	11.34	1.19	1.80	5.6	16	2.00

Table 2 Simulation parameters.

Parameters	Values	
Box size, $m \times m$	0.2942×0.2942	
Time step	$1 \times 10^{-7} \text{s}$	
Granular particle numbers	2400	
Granular particle radius	$3.026 \times 10^{-3} \text{ m}$	
Number of SPH particles per disk	61	
SPH Particle radius	$3.4868 \times 10^{-4} \text{m}$	

granular assemblies has been studied in the past. However, most of these systems involve shear [7–10], vibration [11,12] or biaxial strain [13]. In the present study, the granular system is cyclically and isotropically compressed with small strain steps, starting from a packing fraction below jamming, to a packing fraction above jamming. The Smoothed Particle Hydrodynamics (SPH) method is used to simulate the interaction of granular particles. Each granular particle is made up of several SPH particles which can accurately account for the stress generated within each granular particle. In addition, contact forces are calculated using an advanced formulation that accounts for the contact geometry and force distribution around the contact area. A brief validation of the simulation method used is also provided in the paper.

2. Methods and physical models

In this paper the granular materials are simulated using the Smoothed Particle Hydrodynamics (SPH) method [14–17]. The SPH is a meshless method where the governing equations are solved by discretizing the two-dimensional granular particles with finite number of SPH particles that carry individual mass and occupy certain space. These SPH particles are the mathematical interpolation point themselves. The material properties of the SPH particles are calculated from their relationship with neighboring particles using the kernel function for interpolation. The mass, momentum and energy conservation equations come from continuum mechanics model and are given as:

$$\frac{D\rho}{Dt} = -\rho \frac{\partial v^{\alpha}}{\partial x^{\alpha}} \tag{1}$$

$$\frac{Dv^{\alpha}}{Dt} = \frac{1}{\rho} \frac{\partial \sigma^{\alpha\beta}}{\partial x^{\beta}} \tag{2}$$

$$\frac{De}{Dt} = \frac{\sigma^{\alpha\beta}}{\rho} \frac{\partial v^{\alpha}}{\partial x^{\beta}} \tag{3}$$

where ρ the density, v^{α} the velocity component, $\sigma^{\alpha\beta}$ the total stress tensor, and e is the specific internal energy.

The SPH approximation for mass, momentum and energy equation take the following form [18],

$$\frac{D\rho_i}{Dt} = \sum_{i=1}^{N} m_j \left(v_i^a - v_j^a \right) \frac{\partial W_{ij}}{\partial x_i^\alpha} \tag{4}$$

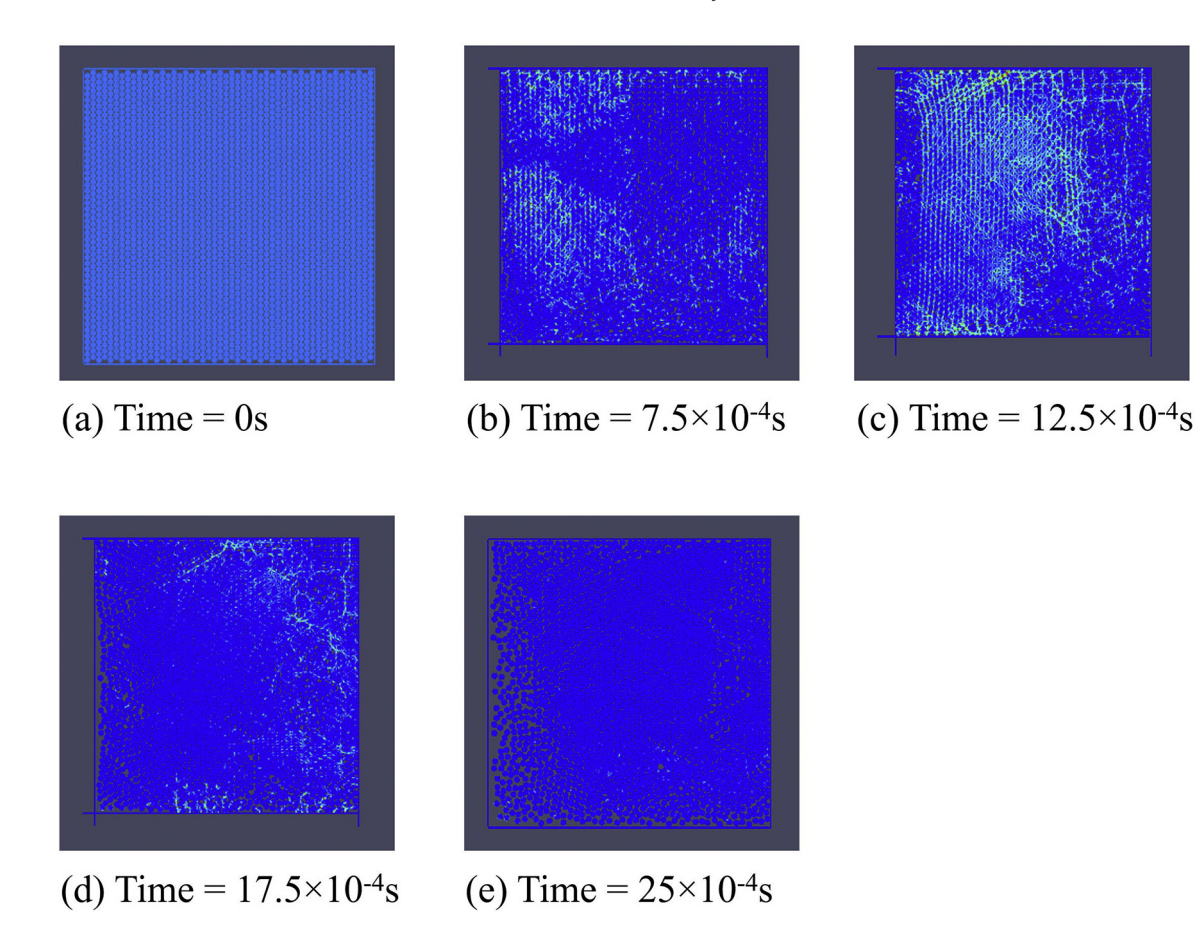


Fig. 1. One full cycle of compression and expansion showing also the force chain networks.

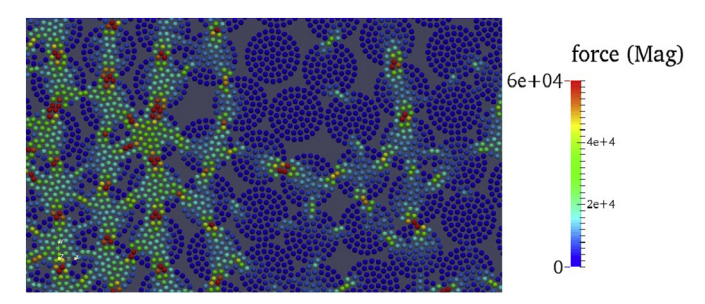


Fig. 2. A closer look of the disks and force chains.

$$\frac{Dv_i^{\alpha}}{Dt} = \sum_{j=1}^{N} m_j \left(\frac{\sigma_i^{\alpha\beta}}{\rho_i^2} + \frac{\sigma_j^{\alpha\beta}}{\rho_j^2} \right) \frac{\partial W_{ij}}{\partial x_i^{\beta}}$$
 (5)

$$\frac{De_i}{Dt} = -\frac{1}{2} \sum_{j=1}^{N} m_j \left(\frac{\sigma_i^{\alpha\beta}}{\rho_i^2} + \frac{\sigma_j^{\alpha\beta}}{\rho_j^2} \right) \left(v_i^a - v_j^a \right) \frac{\partial W_{ij}}{\partial x_i^\beta} \tag{6}$$

where m is the mass of individual particle and W_{ij} is the kernel function. Several different kernel functions have been used in the SPH literature. The most popular one is the cubic spline function proposed by [19], which has the following form:

$$W(R,h) = \alpha_d \times \begin{cases} \frac{2}{3} - R^2 + \frac{1}{2}R^3 & 0 \le R < 1\\ \frac{1}{6}(2 - R)^3 & 1 \le R < 2\\ 0 & R > 2 \end{cases}$$
 (7)

where α_d is the normalization factor which is $15/7\pi h^2$ in twodimension, h is the smoothing length and R is the distance between particles i and j normalized as R = r/h. Unlike DEM where the contact forces are the main simulation variable and stress within particles are unknown, the SPH solution produces density, velocity, stress, and strain at each timestep directly. Constitutive models for stress and strain for actual materials can also be directly implemented in the SPH method.

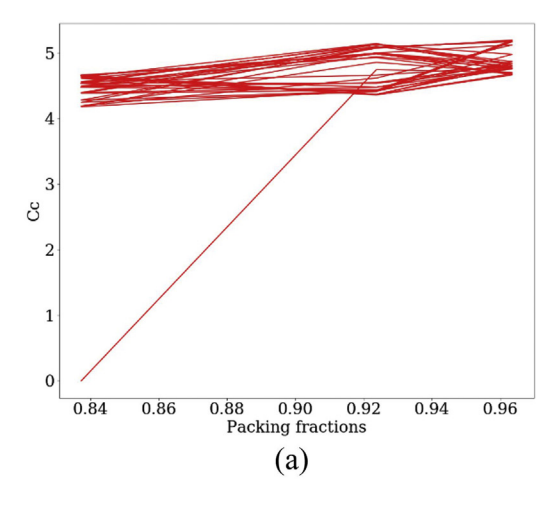
The SPH method used in this study is improved to include certain terms in the discretized governing equations to better numerical stability. One of those terms is the artificial viscosity term added to the momentum equation to prevent large unphysical oscillation in the numerical solution and improve numerical stability. There are several variations of the form of artificial viscosity exist in the SPH literature. The one used here is the most popular one proposed by Monaghan [20]. The artificial stress method proposed by Monaghan [21] and

Grey et al. [22] to remove the problem of tensile instability, which can occur in SPH, is also used in this study. The velocity smoothing technique [15] is used to smooth out any unexpected numerical peaks in the velocity. The smoothed velocities are used to update the position of the particles, while the unsmoothed velocities are used for time integration of the momentum equation at the following step.

Interactions between granular particles are modeled by a kinematic contact algorithm developed by [23] for low velocity impact problem for SPH. The weak form of the contact force equation is derived using the virtual work principal and is solved by a penalty method that involves both a penetration and a penetration rate for two particles in contact. The relation between contact force and penetration and penetration rate is obtained using a one-dimensional elastic wave equation [23]. In order to apply the contact force model, a contact detection technique is needed to identify the boundary SPH particles. To find the boundary particles, a color parameter, ψ_i is introduced for each SPH particles. A particle will be designated as a boundary particle if the summation of ψ_i is less than 0.85–0.90 of the original index value [23,24]. Usually SPH particles are imaginary interpolation points that are used to decompose the simulation domain. Here, the SPH particles are treated like a real particle and each has a radius that is equal to half the lattice or center to center spacing. Two particles are in contact if the center to center distance between two SPH particles is less than their respective diameters. To obtain the penetration and penetration rate for two SPH particles in contact, the curvature of the surface needs to be taken. One way to obtain the curvature is to calculate the gradient of the color parameter, ψ_i . The penetration depth can be found by taking component of the center to center distance along the average normal vector for the two surfaces in contact. The penetration rate is found from the relative velocity and the average normal vector [23]. The force of contact is then found from the penetration and penetration rate of the two SPH particles.

In this paper the Mie-Gruneisen equation for solids [25] is used to calculate the pressure arising from the deformation of the material. Table 1 gives the material properties and constants for Mie-Gruneisen equation of state for lead, which is the material chosen for simulation, where ρ_0 is the density, c is the speed of sound in the material, E and G are respectively bulk and shear moduli and S and Γ are material parameters needed to calculate the Mie-Gruneisen equation of state. The stress rate obtained from the constitutive relation must be invariant with respect to rigid body rotation when large deformation is involved. The Jaumann stress rate is adopted for this purpose as,

$$\dot{s}^{\alpha\beta} - s^{\alpha\gamma}\dot{R}^{\beta\gamma} - s^{\gamma\beta}\dot{R}^{\alpha\gamma} = 2G\dot{e}^{\alpha\beta} \tag{8}$$



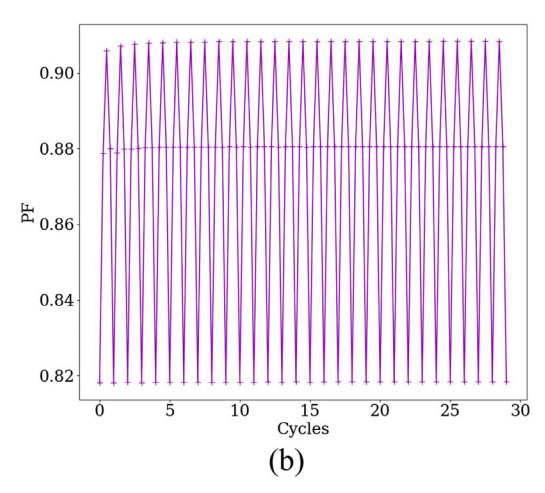


Fig. 3. (a) Corrected coordination number vs packing fraction for all cycles. (b) Packing fractions change with loading cycles.

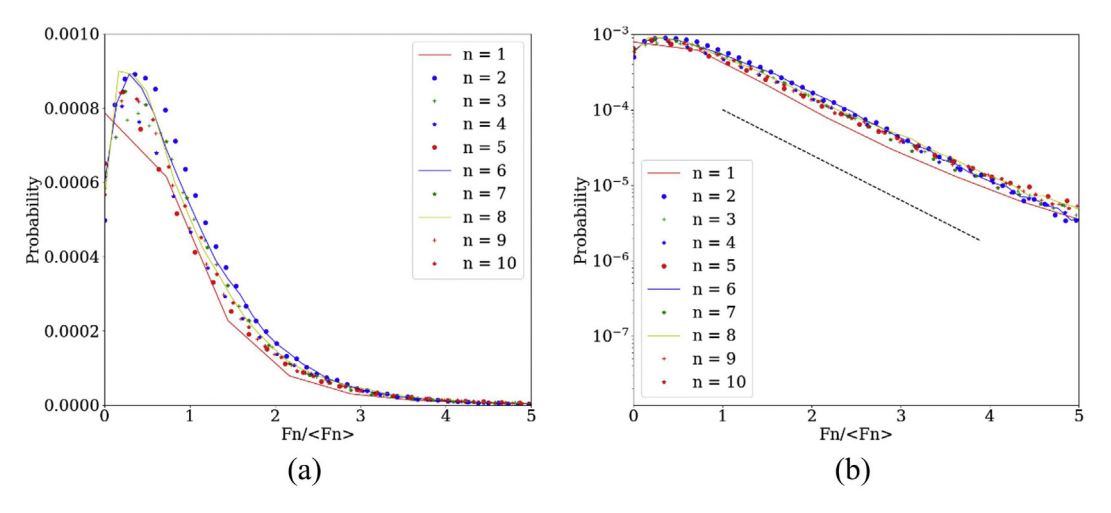


Fig. 4. Probability distribution of the normalized contact forces shown in (a) linear and (b) semi-log scale. The forces are normalized by the mean force. The dashed black line in (b) is added as a visual guide only.

where $\dot{R}^{\beta\gamma}$ is the rotation rate tensor defined as,

$$\dot{R}^{\beta\gamma} = \frac{1}{2} \left(\frac{\partial v^{\beta}}{\partial x^{\gamma}} - \frac{\partial v^{\gamma}}{\partial x^{\beta}} \right) \tag{9}$$

and $\dot{R}^{\alpha\gamma}$ has the same equation except β is replaced by α .

At the beginning of simulation 2400 mono-sized disks are placed within the two-dimensional square box. The box size, disk size and their material properties are given in Tables 1 and 2. The disks are placed such that there is no initial contact with the wall of the container or among the disks. The initial packing fraction for the system is 0.8. Gravity is neglected in this study. Two sides of the container are kept stationary while the two other sides are displaced with a linear velocity. The left and bottom walls move backward and forward with an amplitude of 20 mm in each cycle (see Fig. 1). The time period for the cycle is 2.5 millisecond. However, each cycle consists of several steps where the walls are kept stationary to relax the system. The time step used for the simulation is 0.1 microsecond. The moving walls perform several compression cycles where the system is quasi-statically compressed or expanded.

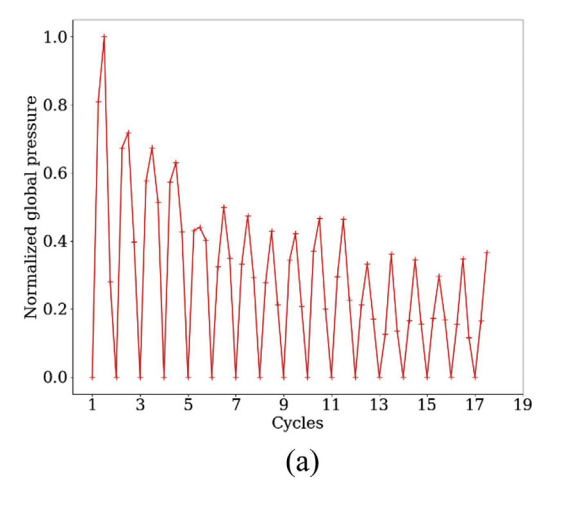
Fig. 2 gives a closer view of the disks and the force chains. Each disk consists of 61 SPH particles arranged in an optimum packing configuration [26]. The radius of each SPH particle is about 0.35 mm. The walls are also made of SPH particles. For the case of walls square lattice

configuration is used and the lattice spacing is twice that of the SPH particle radius. Each wall has two layers of SPH particles.

3. Results and discussion

3.1. Coordination number, packing fraction and distribution of contact forces

For a granular system to reach mechanical equilibrium or "jammed," the system needs to satisfy a minimum number of contacts that is theoretically related to the degrees of freedom of the system. The isostatic conjecture [27–33] for frictionless system of N particles in dimension D states that for mechanical equilibrium there must be at least Z=2Dcontacts on average per particle (since there are NZ/2 independent forces and DN force balance constraints). However, the average coordination number from simulation or experiment is usually lower than 2D due to the presence of rattlers, which are particles that do not contribute to the force chain. They may have zero or some contacts but those contacts do not add to the mechanical stability of the packing. One way to identify rattlers is to count their contacts. For this frictionless simulation case, particles with less than four contacts are defined as rattlers [34–39]. The corrected coordination number, Cc, which is the ratio of the total number of contacts of particles with at least 4 contacts and the number of those particles, shown in Fig. 3 (a), follows perfectly the isostatic conjecture. The only zero value of Cc is recorded at the



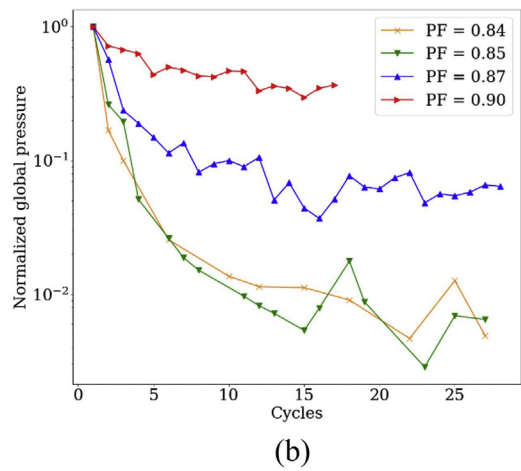


Fig. 5. Pressure evolution over the compression cycles with normalized global pressure shown in (a) linear scale for PF = 0.85 and (b) log scale for different PFs.

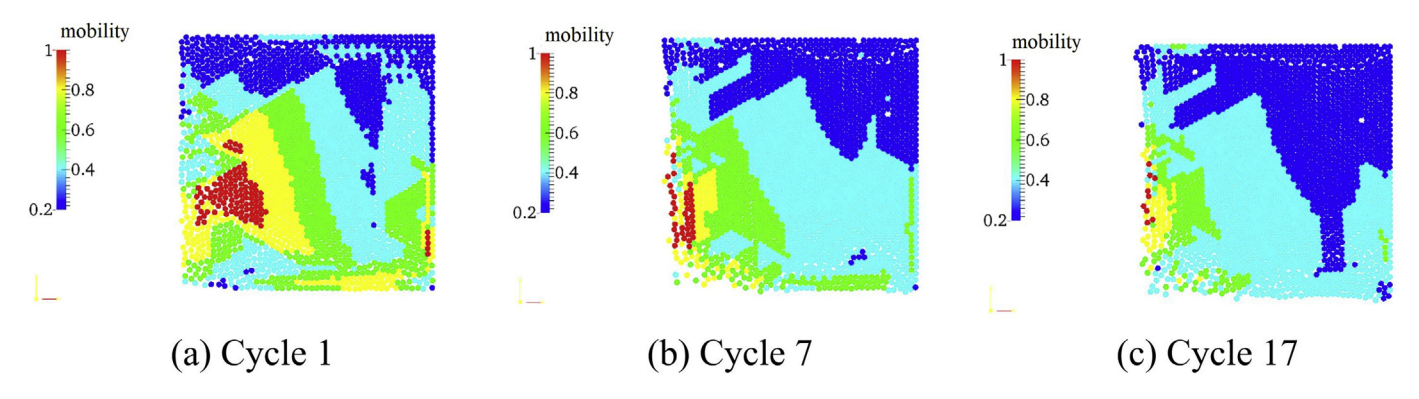


Fig. 6. Mobility of the particles (disks) for different cycles. The initial packing fraction of the system is $\phi = 0.8$. The time delay τ equals (a) 1 cycle (b) 7 cycles and (c) 17 cycles.

beginning when there is no contact. On the other hand, Fig. 3 (b) shows the nice and regular oscillations of the average packing fraction as the system is compressed to a maximum value and expanded. Here the system is compressed to a maximum value of 0.91.

The distribution of contact forces for different compression cycles is shown in Fig. 4. Unlike DEM where the force acts at a single point, in SPH the contact force for a single granular particle is found by integrating forces on the individual SPH particles over the area of contact. Previous studies [40] of granular materials have pointed out that the probability distribution of contact forces decreases exponentially with increase of contact forces, Fn, above the average value, <Fn>. The data shown in Fig. 4 for a packing fraction of 0.91, show, this, indeed is the case for present simulation. A black dashed line is added in Fig. 4 (b) to aid in visualization. The force distributions for all cycles fall on a nearly straight line in the semi-logarithmic plot for probability distribution indicating that the probability distributions of the normalized contact forces follow nearly an exponential decay, which is consistent with previous studies [40]. Fig. 4 (a) and (b) also show that the force distributions are nearly constant for loading cycles.

3.2. Global pressure response

The global pressure on the granular system is computed by first computing the Cauchy stress tensor for the granular system. The Cauchy stress is given by [41]:

$$\sigma_{ij} = \frac{1}{2Area} \sum (F_i x_j + F_j x_i) \tag{10}$$

where Area is the area of the confining container; F_i , F_j are the components of the concentrated force F on the boundary that is applied on

the disks at points (x_i, x_j) . The summation is taken over all such forces. Pressure, p, is then the trace of the stress tensor.

Global pressure response of the system shown in Fig. 5 where the total normalized pressure for a packing fraction of 0.85 is shown in Fig. 5(a). Fig. 5 (b) indicates pressure, normalized by maximum, for the most compressed states only for different packing fractions. As can be seen, the global pressure decreases with compression step. Fig. 5 (b) shows that the global pressure evolves differently for different packing fractions. For packing fraction of 0.9 the global pressure shows very little change with change compression steps whereas lower packing fractions show remarkable change in the global pressure. It can be noted that for all packing fractions in this study, the system is jammed during part of each cycle, however, the stress relaxes to a somewhat lower value. This may be because the cyclic compression of the disks allows the entire structure to slowly rearrange themselves and attain a state of less global pressure for same packing fraction. The next and subsequent part of this paper focused on finding the origin of this evolution of the global pressure.

3.3. Bulk structural change and dynamic heterogeneity

The global stress evolution in the granular system can be associated with bulk structural change within the assembly. If such a bulk rearrangement exists, then it is expected to show up in the motion of the particles tracked over time or cycles. To probe the effect of particle motion, the mobility of particles is considered; it is defined as the displacement of the particle for a given time delay τ (here, time represents the number of compression cycles), relative to the mean displacement of all particles. Fig. 6 shows mobilities for three different time delays, $\tau=1, \tau=7$ and $\tau=17$, in compression simulation on disks. Particles with similar mobility are represented by similar colors in Fig. 6.

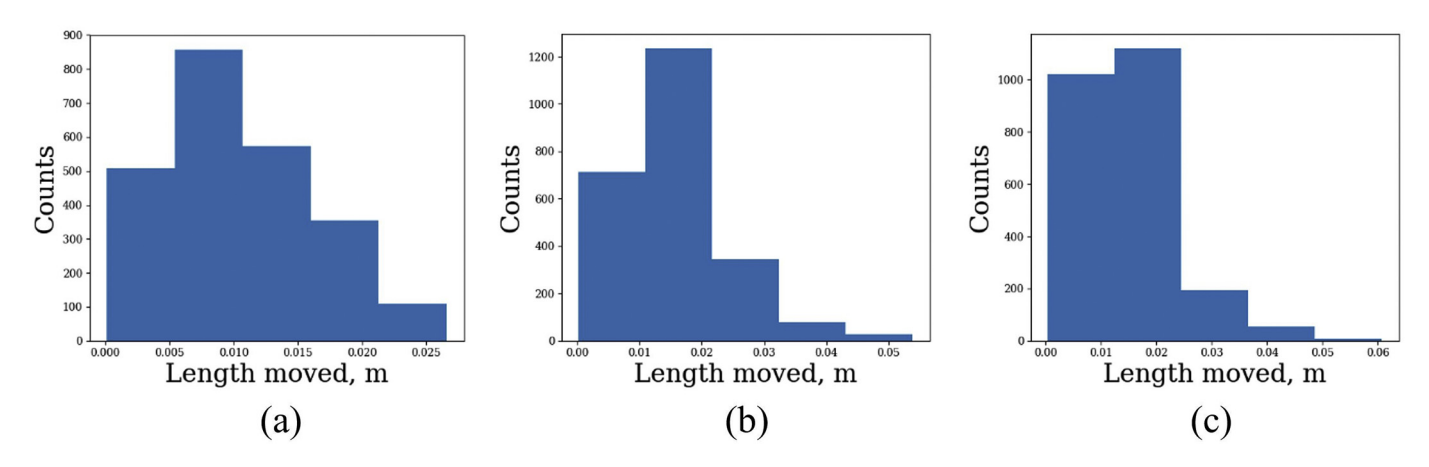


Fig. 7. Histogram of the mobility of the particles (disks) for different cycles. The initial packing fraction of the system is PF = 0.8. The time delay τ equals (a) 1 cycle (b) 7 cycles and (c) 17 cycles.

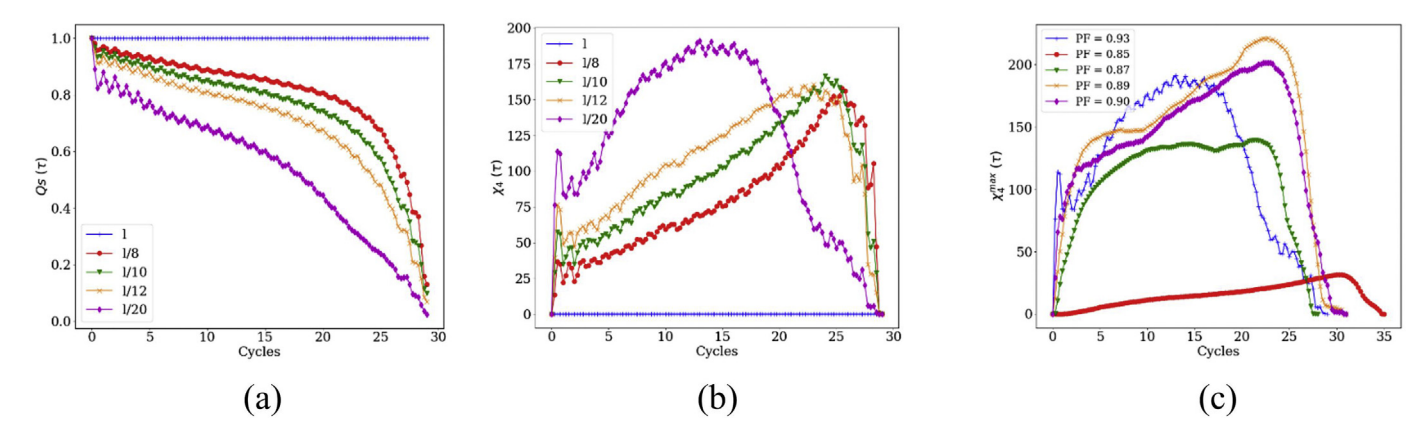


Fig. 8. (a) $Q_s(\tau)$ vs cycles for packing fraction 0.93. (b) $\chi_4(\tau)$ vs cycles for packing fraction 0.93. (c) Maximum $\chi_4(\tau)$ curve for different packing fractions (PF).

Specifically, the colors correspond to the following fractional changes relative to all the particles: red, 0.90 \pm 0.1; yellow, 0.70 \pm 0.10; green, 0.50 \pm 0.10; cyan, 0.30 \pm 0.10; and blue, 0.10 \pm 0.10.

The particle mobility, shown in Fig. 6, reveals that particles with similar mobility form large clusters and these clusters or regions grow with time. This indicates heterogeneous structural change both in time and space. The dense structure of these clusters suggests small local rearrangements of the particles. The number of particles with least mobility increases with time whereas particles with highest mobility decrease; however, this change occurs in a collective form which further suggests local rearrangement of particles. Fig. 7 shows the histogram of the particles based on their mobility for the given cycles, which also confirms the above observations.

As an alternative approach to quantifying these heterogeneous dynamics, the four-point susceptibility $\chi_4(\tau)$, which indicates the extent of temporal correlation of dynamics at any pair of spatial points is studied [1]:

$$\chi_4(\tau) = N \left[\left\langle Q_s(\tau)^2 \right\rangle - \left\langle Q_s(\tau) \right\rangle^2 \right] \tag{11}$$

where $Q_s(\tau)$ is defined as

where N is the number of particles, and $r_i(t)$ indicates the particle positions at time t, for a length scale l (the unit of length scale, l, is the radius of the disks). The averages are taken over all the particles and over all starting times. $Q_s(\tau)$, which is referred to as the self-overlap order parameter, is a measure of particle mobility and is quantified by a length

scale $l. Q_s(\tau)$ and $\chi_4(\tau)$ vs cycles are plotted in Fig. 8 (a) and (b), respectively. As can be seen, $Q_s(\tau)$ varies from 1 to 0 as the time delay τ increases. On the other hand, $\chi_4(\tau)$ has a maximal point for each length scale, which basically characterizes a time delay τ^* , by which the particles, on average, move more than the length scale l.

As seen in Fig. 8 (b), $\chi_4(\tau)$ is maximum for the characteristic length scale $l^{\dagger} \simeq l/20$ for a packing fraction of 0.93. The characteristic l^{\dagger} for each $\chi_4(\tau)$ plot of different packing fractions can be examined and the corresponding maximal τ^{\dagger} can be found. Fig. 8 (c) shows the maximum $\chi_4(\tau)$ curve for different packing fractions. The plot suggests that the typical length scales for l are just fraction of a particle diameter. Also, the plot provides a characteristic time scale τ^{\dagger} by which the particles, on average, move more than the length scale l. The characteristic time scale, τ^{\dagger} , is typically 25 cycles for any packing fractions. Hence the particles can be considered largely confined. However, their small movement is enough to modify the force network and relax the system stress.

3.4. Structural deformations in compressed states

The heterogeneous dynamics study in the previous section inspires a deeper look at the meso-scale structural change that can give rise to change in global stress. On such an endeavor, the granular system is probed using Falk-Langer [42] measures of affine and non-affine deformations. A cutoff radius of 2.5d is used for the FL analysis. This typically includes 10–15 neighboring particles, including the particle of interest. The deformation of these particles is followed for a time equal to τ^\dagger obtained from the previous study.

Unlike FL analysis, the particles displacements are measured with respect to the center of mass of the assembly within the cutoff radius. If r_i and $r_{i'}$ are the locations of all the particle i with respect to the center of mass of the assembly for the initial and final steps then a 2×2 matrix,

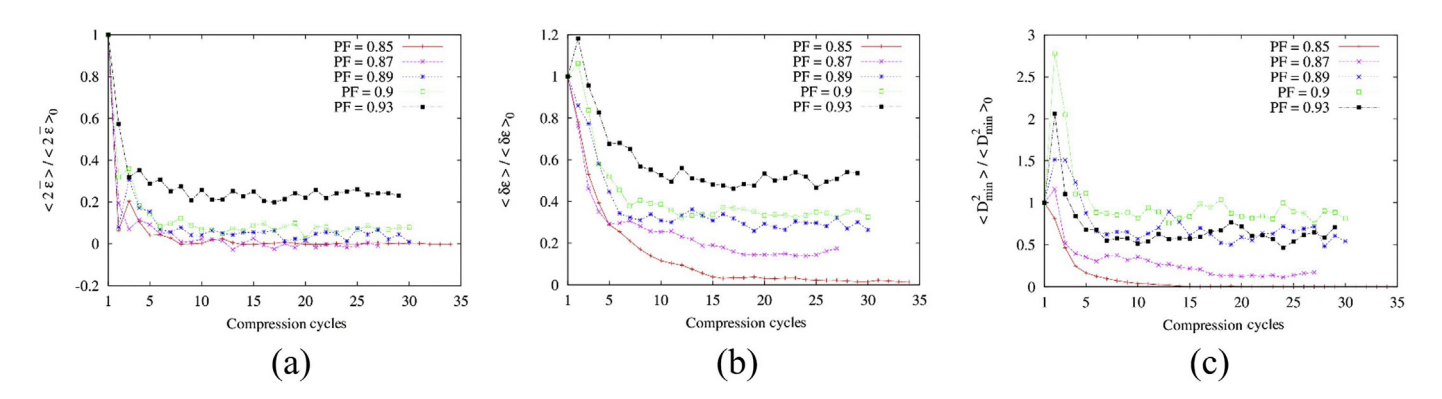


Fig. 9. Deformation of the particles for different cycles (a) normalized average affine dilation (b) normalized average affine shear strain (c) normalized non-affine mean squared displacement.

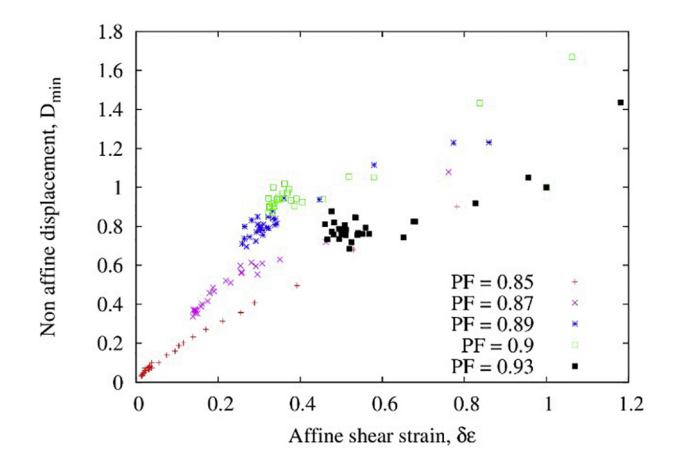


Fig. 10. Correlation of affine and non-affine deformations for various packing fractions.

E' can be obtained from the least-square fit of the equation:

$$r_i' = E' \cdot r_i \tag{13}$$

The matrix E is the best-fit linear map that affinely transforms the particles from the first position to the next one. The matrix E' can be

written in terms of a symmetric matrix, F, and a rotational matrix, R_{θ} , as,

$$E' = FR_{\theta} \tag{14}$$

From the symmetric matrix, *F*, the strain matrix can be obtained as,

$$\varepsilon = F - I \tag{15}$$

The affine shear strain and affine deformation can then be obtained from the eigenvalues (ε_1 and ε_2 where $\varepsilon_2 \ge \varepsilon_1$) of the local strain matrix, ε :

Affine shear strain :
$$\delta \varepsilon = \varepsilon_2 - \varepsilon_1$$
 (16)

Affine dilation :
$$2\overline{\varepsilon} = \varepsilon_1 + \varepsilon_2$$
 (17)

Non-affine deformation can be obtained as : D_{\min}

$$= \left(\sum \left(r_i' - E \cdot r_i\right)^2\right)^{\frac{1}{2}} \tag{18}$$

Fig. 9 represents data for affine and non-affine deformations for different packing fractions over several compression cycles in the granular system. The deformation data presented are summed over all particles and normalized by their initial mean value. Both affine and non-affine deformations fall quickly to a fixed value and fluctuates around it. The rate of decrease of normalized average affine shear strain is much higher for lower packing fractions than that for higher packing fractions. This possibly suggests a much longer relaxation time scale for systems

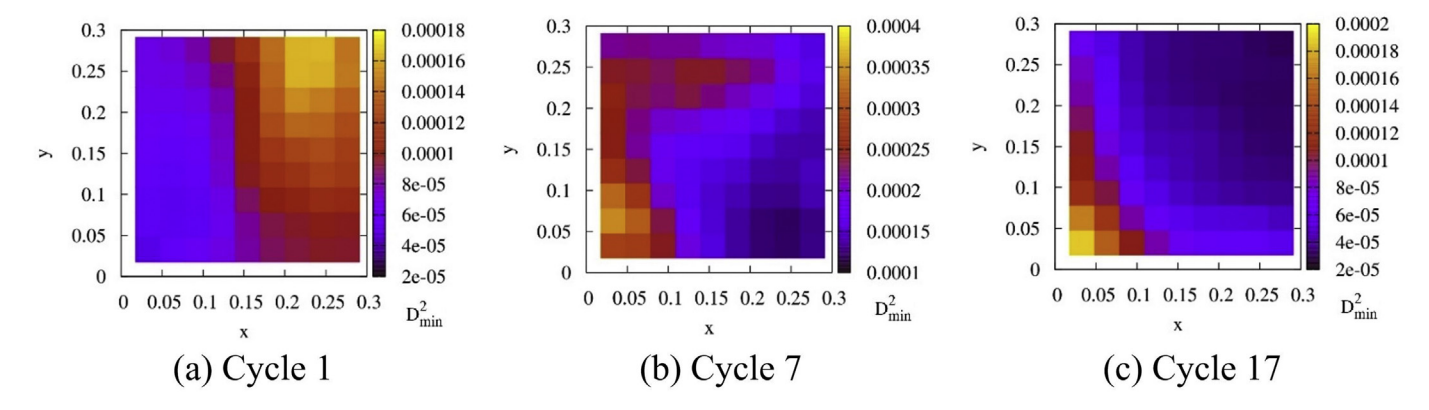


Fig. 11. Intensity plots of D_{\min}^2 for various cycles during simulation. The data shown are for packing fraction, $\phi = 0.87$. Darker (blue) regions indicate low D_{\min}^2 and brighter (red) regions indicate high D_{\min}^2 . (For interpretation of the references to color in this figure legend, the reader is referred to the web version of this article.)

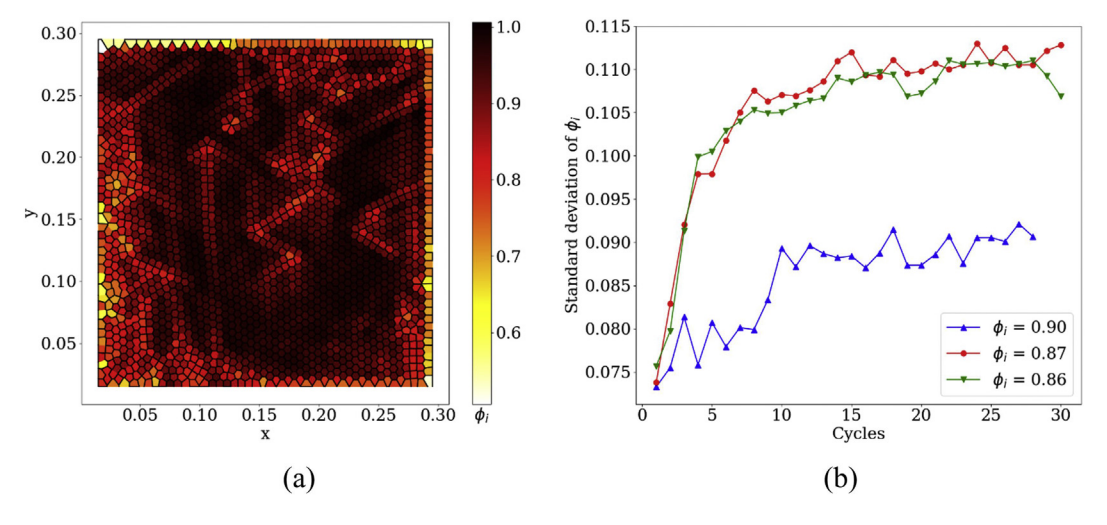


Fig. 12. (a) Voronoi tessellation and local packing fraction shown colored by magnitude (b) standard deviation of local packing fraction for different load cycles.

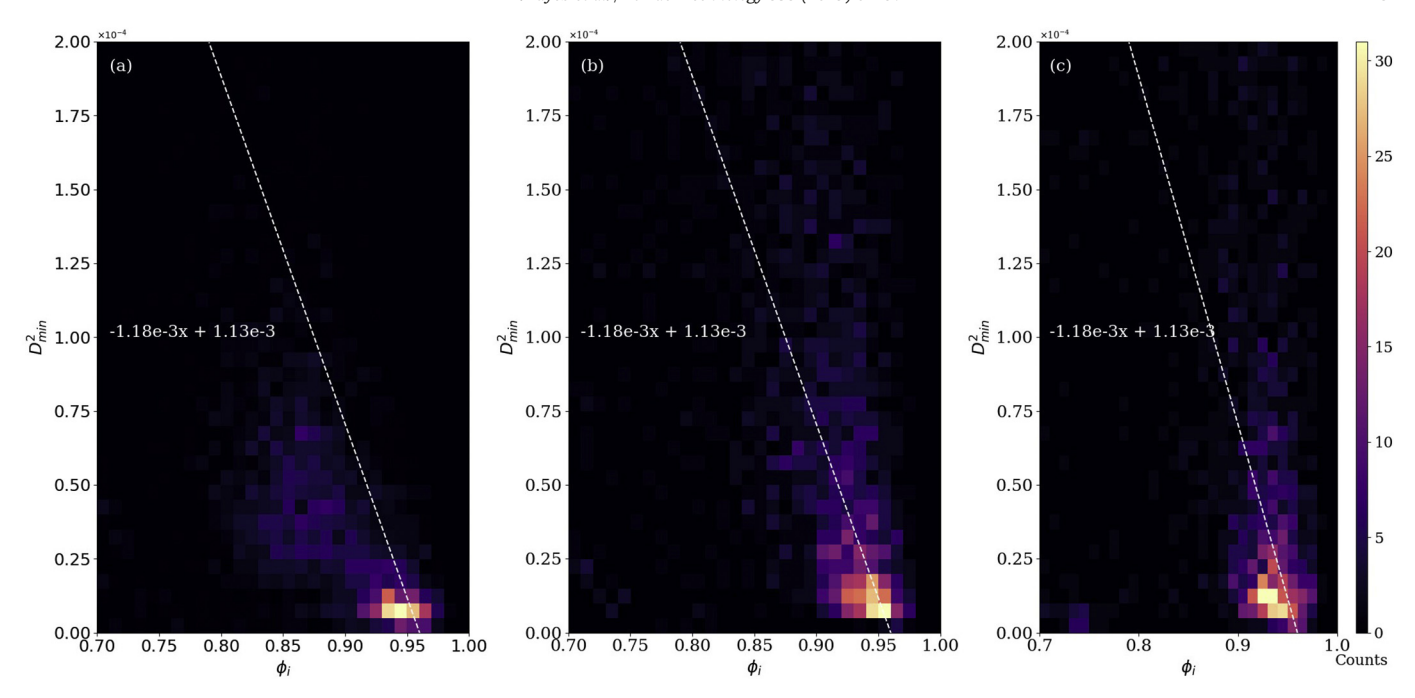


Fig. 13. Density plot of D_{\min}^2 and ϕ_i for different cycles (a) 3 cycles (b) 7 cycles (c) 11 cycles. The dashed white lines are given as a visual guide but are not best fit of the data.

with higher packing fractions. Similar trend is observed for normalized average affine dilation. The higher packing fraction of the system allows the particles to dilate and maintain their deformation. As for the normalized non-affine squared displacement the trend is not so clear. For packing fraction below 0.89 the graph approaches zero quite rapidly. However, for higher packing fractions the graph fluctuates around a mean value suggesting that the non-affine deformation persists throughout the entire loading cycles.

The affine and non-affine deformations are also correlated, which is demonstrated in Fig. 10 The graph suggests that there is a monotonic increase in non-affine displacement with affine shear strain. However different packing fraction occupy different areas of the graph with some overlap. This suggest a relation between systems of different packing fractions.

The intensity plot of the non-affine mean squared displacement is shown in Fig. 11 for three different cycles revealing regions with higher non-affine deformations compared with the rest of the system. At the beginning of loading cycle, most non-affine deformations occur away

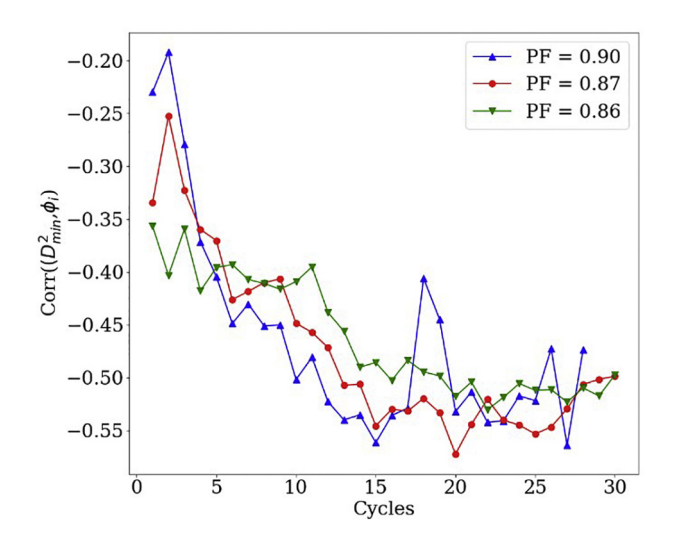


Fig. 14. Correlation coefficient for D_{\min}^2 and ϕ_i at each load cycle for various packing fractions

from the moving walls. As the number of compression cycles increases the non-affine deformations occur more near the wall as indicated by the dark (blue) region in the intensity plot for higher cycle. Fig. 11 can be compared with Fig. 6 where the particles are categorized by their mobility. At the beginning of loading cycle particles near the wall move with the wall and affine deformation presides over non-affine deformation. The particles at the top right corner are forced to rearrange themselves in a more compact structure, thus more non-affine deformations occur at that region. For higher cycles, the particles at the top right can do little in terms of structural rearrangement so the non-affine deformation zone moves down near the walls where particles with higher mobility still have some room to rearrange themselves into more compact structures.

3.5. Linking initial micro-structure to plastic rearrangement

The non-affine deformations as discussed in previous section give rise to plastic rearrangement of the particles in the structure. This plastic rearrangement causes a change in the global stress response of the system. In this section the non-affine deformations of the particles are studied by relating it to the initial micro-structure. More specifically, the question addressed in this section is whether one can predict the global response of the system having prior information about the initial micro-structure (local packing fraction).

First, to get the local packing fraction, the entire system is decomposed into Voronoi cells with radical Voronoi tessellation method. For this purpose, the efficient "pyvoro" software is used developed by Joe Jordan which is a python extension of "voro++" code developed by Chris Rycroft [43]. A sample of the Voronoi tessellation is shown in Fig. 12 (a). The local packing fraction at each loading cycle is then calculated by the formula,

$$\phi_i = \frac{V_i}{V_c} \tag{19}$$

where ϕ_i is the packing fraction around each particle i, V_i is the area of particle i and V_c is the area of the Voronoi cell around particle i. The local packing fraction field is shown in Fig. 12 (a) where the intensity of the color in each cell varies according to the relative packing density. One can immediately recognize from the figure that not all areas have

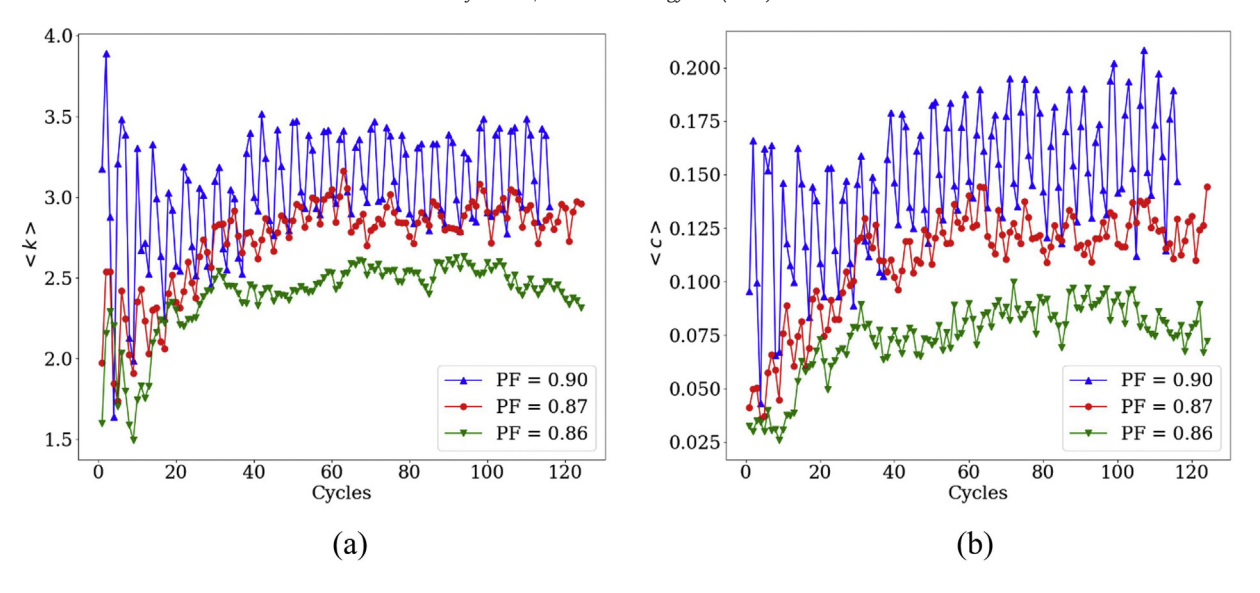


Fig. 15. (a) Average degree vs cycles. (b) Average clustering coefficient vs cycles.

the same packing density. There are regions of high and low local packing fraction. The standard deviation of local packing fraction for different global packing fraction is also shown in Fig. 12 (b). The standard deviation for different cycles is very similar for global packing fraction 0.86 and 0.87 but very different from 0.90. The standard deviation for all three rises with loading cycles and approaches a maximum value. As the walls press down on the particles during loading cycle the average packing fraction of the granular system increases and reaches a maximum value. However due to particle rearrangement in subsequent loading cycles the local packing fractions become more diverse as indicates by the increase in standard deviation of the local packing fraction. However, the increase in diversity is not much for PF = 0.90 as for PF = 0.900.86 and 0.87. It can be recalled from Fig. 5 (b) that the global pressure shows negligible relaxation for packing fractions above 0.9. It is worth studying if there is a correlation between the initial micro-structure or local packing fraction distribution and the non-affine plastic deformation of the particles.

Fig. 13 shows three two-dimensional histogram plots of D_{\min}^2 and ϕ_i for PF = 0.87 at 3, 7 and 11 load cycles. A white dashed line is drawn in the plot to help visualize the correlation between the two variables but

is not a best fit of the data. A least-square mean fit is found to be very sensitive to the higher and lower end values. The plots reveal that the two quantities, D_{\min}^2 and ϕ_i , are indeed related. Despite having a significant dispersity in data, a lower value of ϕ_i usually means a higher value of D_{\min}^2 and vice versa.

To further verify the correlation between D_{\min}^2 and ϕ_i , the Pearson correlation coefficient, the standard correlation coefficient for two variables, is calculated for all N=2400 particles.

$$\operatorname{Corr}\left(D_{\min}^{2}, \phi_{i}\right) = \frac{\sum_{i=1}^{N} \left(\left(D_{\min}^{2}\right)_{i} - \left\langle D_{\min}^{2}\right\rangle\right) \left(\phi_{i} - \left\langle \phi_{i}\right\rangle\right)}{\sqrt{\sum_{i=1}^{N} \left(\left(D_{\min}^{2}\right)_{i} - \left\langle D_{\min}^{2}\right\rangle\right)^{2}} \sqrt{\sum_{i=1}^{N} \left(\phi_{i} - \left\langle \phi_{i}\right\rangle\right)^{2}}} \quad (20$$

where $(D^2_{\min})_i$ means the non-affine squared deformation for particle i, and $\langle \rangle$ means average value. No correlation is indicated if the correlation coefficient is 0 and -1 means perfect negative correlation. The correlation coefficient for all load cycles and for three different packing fractions is shown in Fig. 14. The correlation coefficient increases somewhat monotonically in negative value after the first load cycle

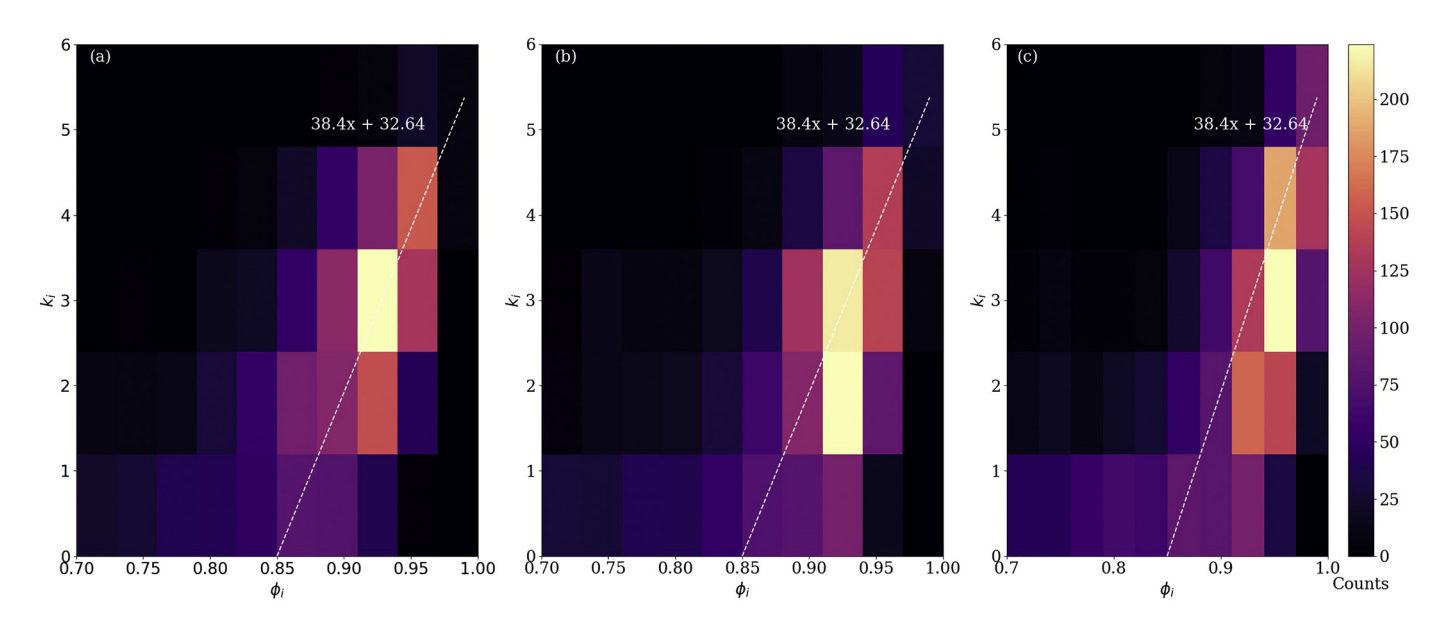


Fig. 16. Density plot of k_i and ϕ_i for different cycles (a) 3 cycles (b) 11 cycles (c) 19 cycles. The dashed white lines are given as a visual guide but are not best fit of the data.

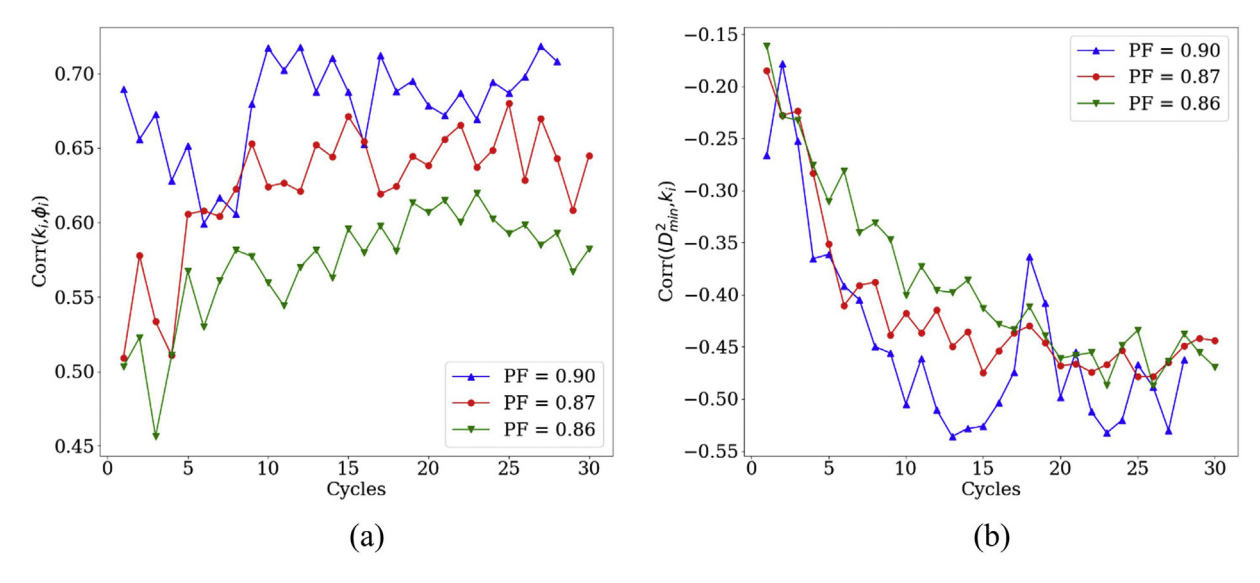


Fig. 17. (a) Correlation coefficient for k_i and ϕ_i and (b) correlation coefficient for D_{\min}^2 and k_i at each load cycle for various packing fractions.

and reaches a maximum of about -0.55. The plot confirms the negative correlation between D_{\min}^2 and ϕ_i suggested by Fig. 13. The negative correlation suggests that particles with low local porosity undergo more non-affine plastic deformation than others. Interestingly, the correlation coefficients are very similar for different packing fractions. However, from Fig. 12 (b) it is seen that the standard deviation for packing fraction 0.90 is much lower than that for other packing. At high global packing fraction the local packing density field is more uniform than for low global fraction. This allows one to make connection between global packing fraction and stress relaxation in terms of the non-affine plastic deformation. For higher packing fractions there are not enough particles with low local packing density to undergo plastic deformation and allow the system to relax.

3.6. Contact network analysis

Finally, a contact network analysis is carried out to have a deeper look on the structural rearrangement of the particles based on their connectivity. In contact network analysis each node of the contact network represents an individual particle and a contact between two particles is represented by an edge. The contact network so formed is undirected and unweighted. The contact networks at the beginning of the compression cycles show fewer connections and subnetworks and fewer closed paths compared to the contact network when the system is strongly jammed. The strongly jammed configuration exhibits many closed

path triangles or cycles. In order to quantify the network some complex network parameters are defined below.

In an unweighted complex network the degree of a node is the number of edges adjacent to it, or the number of particles it is in contact with. It can be calculated from the adjacency matrix:

$$k_i = \sum_i a_{ij} \tag{21}$$

where a_{ij} are elements of the adjacency matrix. An adjacency matrix \tilde{A} is a matrix whose non-zero elements a_{ij} are such that $a_{ij}=1$ if nodes or particles i and j are in contact and zero otherwise. The node degree can be averaged over all nodes or particles to give a measure of the average number of contacts per particle. The clustering coefficient gives a measure of the local connectivity of a node by enumerating the number of 3-cycle closed paths or triangles associated with it and its contacting neighbors. It can be calculated from the adjacency matrix as,

$$c(i) = \frac{1}{k_i(k_i - 1)} \sum_{j,h} \sum_{i \in V(i)} a_{ij} a_{jh} a_{hi}$$
 (22)

where k_i is the vertex degree defined above and V(i) is the set of neighboring vertices of i. The clustering coefficient ranges from 0 (no contacting neighbors) to 1 (all particles and their contacting neighbors are fully connected with each other). Each c(i) is averaged over all

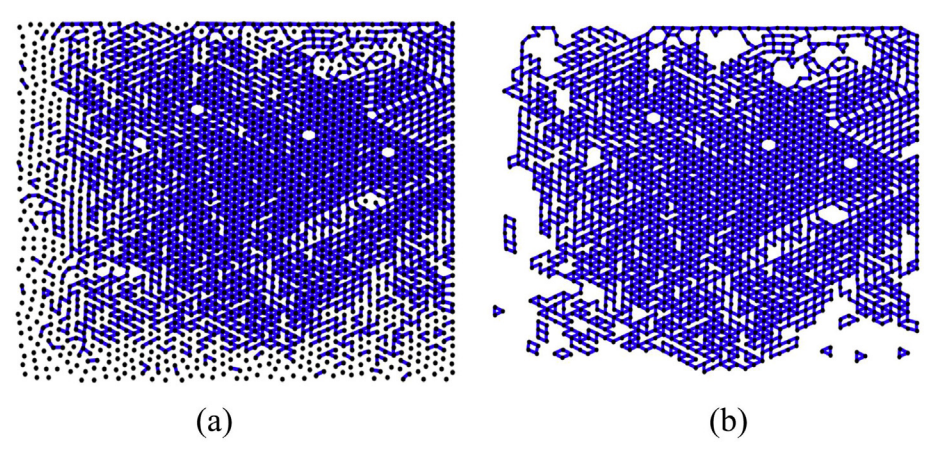


Fig. 18. (a) Contact network with nodes as particles and edges as contacts at 26 compression cycles. (b) Same network with rattlers removed.

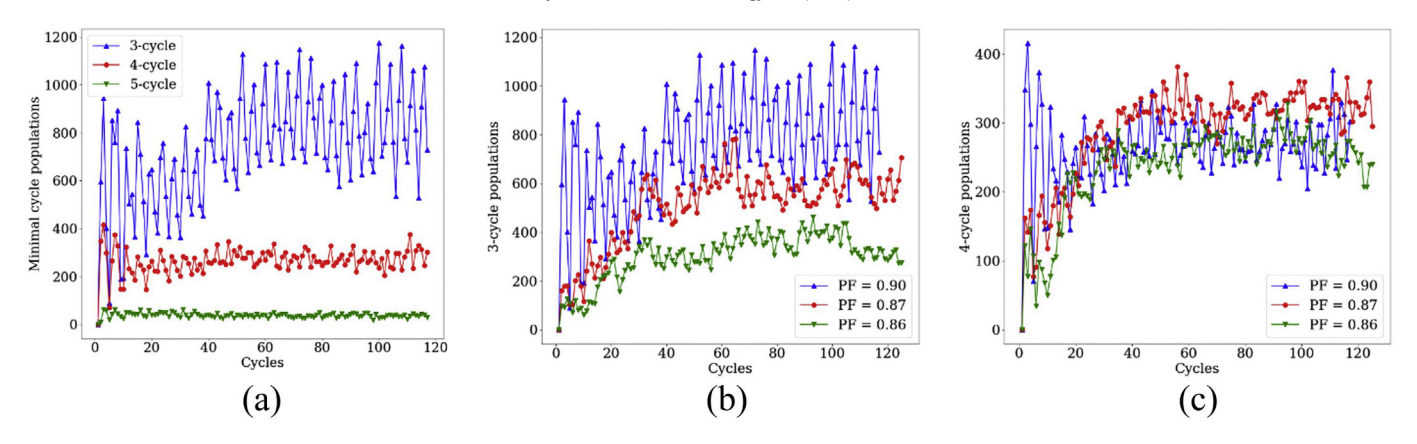


Fig. 19. (a) Population of 3-cycles, 4-cycles and 5-cycles for PF = 0.90. (b) 3-cycle populations only and (c) 4-cycle populations only for all loading cycles for various PF.

particles to obtain the average clustering coefficient which gives an insight about the number of 3-cycles in the network,

The average degree and average clustering coefficient of the contact networks as shown in Fig. 15 (a) and (b). Both plots are created by averaging over all particles in a given load step. The average quantities in both figures show peaks at maximum compression and troughs when fully unloaded. The average degree gradually increases for all global packing fractions with the increase in load cycles showing that the particles are getting more closely packed. For PF = 0.90 the average degree peaks to about 3.5 which is close to the isostatic limit. For other packing fractions the peak values are lower. Similar behavior is ob-

served for average clustering coefficient. Increase in average clustering coefficient means that there are more 3-cycles in the network, which, as found by other researchers, increase the number of force chains in the system [44]. It is also found that the global pressure usually depends on the maximum normal contact force higher than the average force [44]. Hence increase in force chains or force bearing particles means the global pressure can relax for the system.

It would be interesting to investigate if there is a correlation between the local packing fraction defined in the previous section and the degree of particles. One can assume that, since higher the connectivity of the particle higher is its degree, that particles with high degree are situated

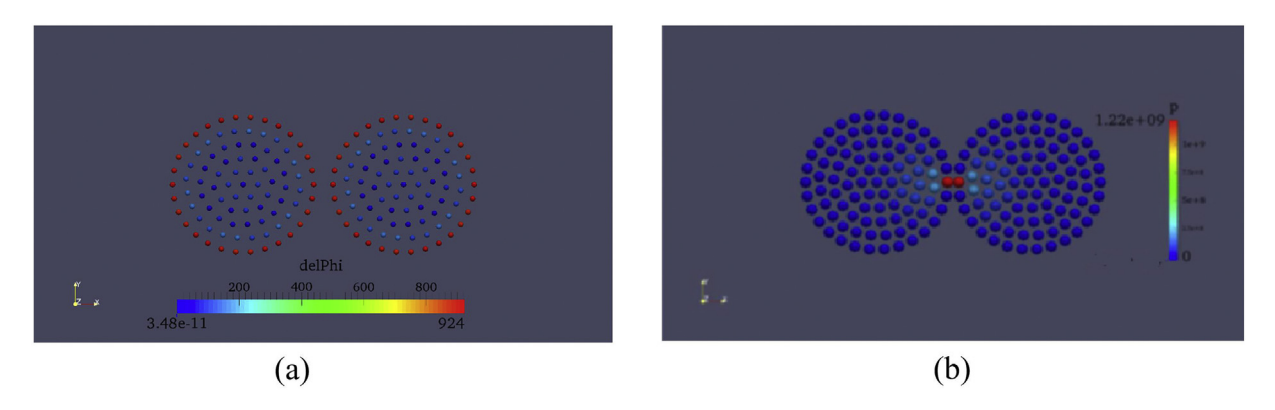


Fig. 20. (a) The boundary particles indicated by color gradient, $\Delta \psi$ (b) Pressure distribution of two colliding disks.

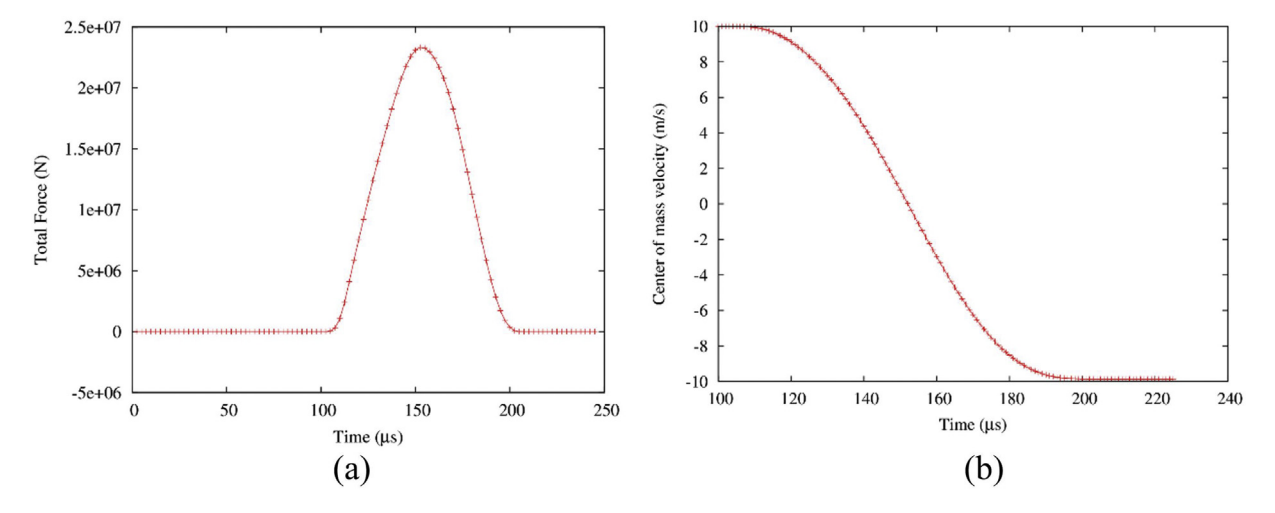


Fig. 21. (a) Total contact force-time histories and (b) average velocity-time history of the two colliding disks.

in a region with high packing fraction. The density plots of Fig. 16 show, this, indeed is the case. Again, the white dashed line is not a best fit of the data but added as a visual guide for the plot. The plots show the relation between the particle degree and local packing fraction for three different load steps, 3, 11 and 19 load cycles.

To further confirm the correlation, the correlation coefficients for k_i and ϕ_i are plotted for each cycle and shown in Fig. 17 (a), which shows that there is a high amount of correlation exists between the two for all cycles. In the previous section it was shown that D_{\min}^2 and ϕ_i are negatively correlated and the correlation coefficient increases with cycles. Fig. 17 (b) shows the correlation coefficient for D_{\min}^2 and k_i for different load cycles. The quantities D_{\min}^2 and k_i are negatively correlated as shown in Fig. 17 (b) which is not surprising given the fact that k_i and ϕ_i are positively correlated. Thus, a connection can be made between the Falk-Langer deformation analysis of Section 3.4 and the complex network analysis of Section 3.6 in that higher non-affine deformation or plastic rearrangement is usually related to particles with lower degree of connectivity and local packing fraction.

It is also worth studying the 3-cycle population of the contact network as they are important in stabilizing the contact network. These cycle structures are found by computing the population of the various minimal cycles in the contact network. A minimal cycle basis of a graph is a set containing the shortest cycles based on minimum length or number of edges. There are several algorithms proposed by other researchers to obtain a minimal cycle basis for a complex network. Here, the fast and improved algorithm based on Mehlhorn and Michail [45] is implemented to find the minimal cycle basis for the contact network. Fig. 18 (a) shows the contact network at 26 compression cycles for PF = 0.90 when the system is strongly jammed. The particles are represented as nodes and contacts as edges. Fig. 18 (b) shows only the minimal cycles of the same network with the rattlers removed.

According to the clustering coefficient, population of 3-cycles and other higher order substructures is expected to peak when the system is in strongly jammed configurations. This is indeed the case as shown in Fig. 19 (a) where the 3-cycle and 4-cycle structures oscillate throughout the loading cycles. Only low-order cycles, namely, 3, 4 and 5 cycles are shown in Fig. 19 (a). Cycles greater than 5 have negligible populations. As shown in Fig. 19 (a) the population of 4 cycles shows oscillations but the oscillations are small compared to 3 cycles and the oscillations of 5 cycles are even smaller. There is a gradual rise in the 3 cycles population throughout the compression cycles at the strongly jammed state indicated by a rise in the peak values of oscillations. This means that the granular systems rearrange themselves in a way which gives rise to more 3-cycles in the network in the jammed state as the number of compression cycle increases.

Fig. 19 (b) and (c) compare the populations of the 3-cycles and 4-cycles for different global packing fraction. The population of 3-cycles rises for all packing fractions and higher packing fractions have higher number of 3-cycles in the network. On the other hand, the populations of 4-cycles are quite similar for the three packing fractions shown in Fig. 19 (c) at higher load cycles. Hence, enrichment of 3-cycle population can be considered as a marker for successive compressive loading of a granular system.

4. Conclusion

In this paper, Smooth Particle Hydrodynamics (SPH) method is used to simulate the cyclic compression of deformable two-dimensional disks assembly and to study their jamming behavior. The results obtained show that the average coordination number varies with packing fraction during jamming which conforms to the isostatic conjecture. Force distribution shows familiar exponential behavior as the average force on the system is increased. Stress relaxation is seen to occur after several compression cycles which is marked by a decrease in global pressure. Structural rearrangement, that can give rise to stress

relaxation, is revealed by grouping of particles with similar relative mobilities and γ_4 measures which also provide a characteristic time scale τ^{\dagger} for which the particles on average move more than a characteristic length scale l^{\dagger} . The meso-scale structural deformations are studied by Falk-Langer analysis. Active regions of non-affine deformations are found and locations of these regions change over cycles. The local packing fraction of the granular system is obtained by employing radical Voronoi tessellation method. The standard deviation of the local packing fraction is seen to increase with load cycle but at a different rate for different global packing fraction. This suggests that the local packing fraction becomes more diverse with increasing compression cycle. For high global packing fraction the diversity is less pronounced. The correlation coefficient between non-affine squared deformation and local packing fraction suggests that the two quantities are negatively correlated for both high and low packing. This infers that at high enough global packing fraction there is not much room for the system to relax its stress state. Finally, complex network analysis is performed to study the contact network properties of the system. The average degree and average clustering coefficient obtained from the complex network analysis show peaks at maximum compressions, but the peak values increase with cycles. The degree per particle is found to be positively correlated with local packing fraction and negatively correlated with the non-affine squared deformation. An enrichment of 3-cycle population is observed for all global packing fraction with increase in compression cycle. Thus the number of 3-cycle population can be considered as an important parameter to characterize the system behavior in cyclic compression of granular system.

Nomenclature

HOIIICITCI	iture
a_{ij}	elements of adjacency matrix
Α	area of contact, m^2
Area	area of the container, m ²
Ã	adjacency matrix
С	sound speed, m/s
c(i)	clustering coefficient of particle
d	diameter of particle, m
D	System dimension
D_{\min}	non-affine deformation
е	specific internal energy, J/kg
Ε	Elastic modulus, Pa
E'	transformation matrix
F	symmetry matrix
F_i	force on particle i, N
$F_{\rm max}$	maximum contact force, N
G	Shear modulus, Pa
h	smoothing length, m
k_i	degree of a node
1	length scale
Į†	characteristic length scale
m	mass of particle, kg
N	number of particles
p	hydrostatic pressure, N/m ²
P	normal contact force, N
PF	packing fraction
Q_s	self-overlap order parameter
r	distance vector, m
r_i	position of particle i
$\stackrel{R}{\dot{R}}^{eta\gamma}$	normalized distance
	rotation rate tensor
R_{θ}	rotational matrix
S	deviatoric stress tensor, N/m ²
t_{max}	time for collision, sec
ν	velocity, m/s
* *	1 6 3

volume of particle, m³

area of Voronoi cell, m²

area of particle i, m²

 V_{c}

distance vector, m x

V(i)set of neighboring vertices

kernel function W

Z average per particle contacts

Greek symbols

normalization factor α_d

β constant

Γ EOS parameter

contact deformation δ

maximum deformation δ_{max}

ε strain matrix

affine shear strain δε

affine dilation 3

EOS parameter

η A angle between normal vectors

penalty parameter λ

equivalent mass ш

poisson ratio ν

П artificial viscosity term

density, kg/m³ ρ

σ stress tensor, N/m²

time delay

characteristic time scale

local packing fraction ϕ_i

four-point susceptibility χ_4

color function

Acknowledgments

Support for this work by the U.S. National Science Foundation under grant number CBET-1404482 is gratefully acknowledged.

Appendix A. Validation of sph model using impact of two identical disks

The above SPH contact model is used to simulate impact of two identical disks each of radius 50 mm and the number of SPH particle in each disk is 91. The material is lead whose properties are given in Table 1. First the contact detection algorithm is tested to see if the boundary particles can be single out from the inner particles. Fig. 20 (a) shows that the boundary particles have a much larger color gradient than the par-

The present results are compared with the Hertz solution for collision of two cylinders of unit length (plane strain problem). Palmgren's [46] empirical result, which expresses the relationship between normal contact force between two cylinders and deformation is given by:

$$P = K\delta^n \tag{23}$$

where n = 10/9.

$$K = \frac{1}{1.36^{n}} E^* L^{8/9} \tag{24}$$

where

$$\frac{1}{E^*} = \frac{1 - \nu_1^2}{E_1} + \frac{1 - \nu_2^2}{E_2}$$

where δ is the deformation. Applying Newton's 2nd law and Palmgren's contact force relation, the maximum deformation and maximum force due to impact can be calculated as:

$$\delta_{\text{max}} = \left(\frac{n+1}{2} \frac{\mu}{K} v_0^2\right)^{\frac{1}{n+1}}$$

$$F_{\text{max}} = K \left(\frac{n+1}{2} \frac{\mu}{K} v_0^2\right)^{\frac{n}{n+1}}$$
(25)

where

$$\mu = \frac{m_i m_j}{m_i + m_j}$$

The time for collision between two disks or cylinder with unit length

$$t_{\text{max}} = \frac{2\delta_{\text{max}}}{\nu_0} \int_0^1 \frac{d(\delta/\delta_{\text{max}})}{\sqrt{1 - (\delta/\delta_{\text{max}})^{(1+n)}}} \tag{26}$$

Fig. 21 (a) shows the total contact force-time history of the impacting disks. The maximum contact force obtained from simulation is 2.30×10^7 N whereas the empirical model gives 2.11×10^7 N. The total contact duration obtained is 97.50 µs as compared to the empirical result of 95.13 μ s.

Fig. 21 (b) shows the average velocity-time history of the two colliding disks. It can be seen that the final rebound velocity is equal to the initial velocity of 10 m/s. Therefore, the kinetic energy is conserved before and after the collision.

References

- [1] C. Thornton, Numerical simulations of deviatoric shear deformation of granular media, Géotechnique 50 (2000) 43-53.
- A.S.J. Suiker, N.A. Fleck, Frictional collapse of granular assemblies, J. Appl. Mech. 71 (2004) 350-358.
- T. Jia, Y. Zhang, J.K. Chen, Simulation of granular packing of particles with different size distributions, Comput. Mater. Sci. 51 (2012) 172-180.
- T. Jia, Y. Zhang, J.K. Chen, Y.L. He, Dynamic simulation of granular packing of fine cohesive particles with different size distributions, Powder Technol. 218 (2012)
- T. Jia, Y. Zhang, J.K. Chen, Dynamic simulation of particle packing with different size distributions, J. Manuf. Sci. Eng. 133 (2011) (021011-021011-021014).
- R. Tayeb, X. Dou, Y. Mao, Y. Zhang, Analysis of cohesive microsized particle packing structure using history-dependent contact models, J. Manuf. Sci. Eng. 138 (2015) (041005-041005-041011).
- S. Farhadi, R.P. Behringer, Dynamics of sheared ellipses and circular disks: effects of particle shape, Phys. Rev. Lett. 112 (2014), 148301.
- D. Howell, R.P. Behringer, C. Veje, Stress fluctuations in a 2D granular couette experiment: a continuous transition, Phys. Rev. Lett. 82 (1999) 5241-5244.
- J.H. Snoeijer, W.G. Ellenbroek, T.J.H. Vlugt, M. van Hecke, Sheared force networks: anisotropies, yielding, and geometry, Phys. Rev. Lett. 96 (2006), 098001. J. Ren, J.A. Dijksman, R.P. Behringer, Reynolds pressure and relaxation in a sheared
- granular system, Phys. Rev. Lett. 110 (2013), 018302. [11] P. Richard, M. Nicodemi, R. Delannay, P. Ribière, D. Bideau, Slow relaxation and com-
- paction of granular systems, Nat. Mater. 4 (2005) 121. [12] P. Philippe, D. Bideau, Compaction dynamics of a granular medium under vertical
- tapping, EPL (Europhys. Lett.) 60 (2002) 677.
- [13] F. Alonso-Marroquín, H.J. Herrmann, Ratcheting of granular materials, Phys. Rev. Lett. 92 (2004), 054301. [14] L.B. Lucy, A numerical approach to the testing of the fission hypothesis, Astron. J. 82
- [15] J. Monaghan, SPH compressible turbulence, Mon. Not. R. Astron. Soc. 335 (2002)
- [16] J.J. Monaghan, An introduction to SPH, Comput. Phys. Commun. 48 (1988) 89–96.
- J.J. Monaghan, Smoothed particle hydrodynamics, Annu. Rev. Astron. Astrophys. 30 (1992) 543-574.
- [18] L.D. Libersky, A.G. Petschek, T.C. Carney, J.R. Hipp, F.A. Allahdadi, High strain lagrangian hydrodynamics, J. Comput. Phys. 109 (1993) 67-75.
- [19] J.J. Monaghan, J.C. Lattanzio, A refined particle method for astrophysical problems, Astronomy Astrophys. 149 (1985) 135-143. [20] J.J. Monaghan, Simulating free surface flows with SPH, J. Comput. Phys. 110 (1994)
- 399–406. [21] J.J. Monaghan, SPH without a tensile instability, J. Comput. Phys. 159 (2000)
- 290-311. [22] J.P. Gray, J.J. Monaghan, R.P. Swift, SPH elastic dynamics, Comput. Methods Appl.
- Mech. Eng. 190 (2001) 6641-6662.

- [23] S. Seo, O. Min, Axisymmetric SPH simulation of elasto-plastic contact in the low velocity impact, Comput. Phys. Commun. 175 (2006) 583–603.
- [24] P.W. Randles, L.D. Libersky, Smoothed particle hydrodynamics: some recent improvements and applications, Comput. Methods Appl. Mech. Eng. 139 (1996) 375–408
- [25] A.G. Petschek, L.D. Libersky, Cylindrical smoothed particle hydrodynamics, J. Comput. Phys. 109 (1993) 76–83.
- [26] B.D. Lubachevsky, R.L. Graham, Curved hexagonal packings of equal disks in a circle, Discrete Comput. Geom. 18 (1997) 179–194.
- [27] F. Radjai, M. Jean, J.-J. Moreau, S. Roux, Force distributions in dense two-dimensional granular systems, Phys. Rev. Lett. 77 (1996) 274–277.
- [28] G. Combe, J.-N. Roux, Strain versus stress in a model granular material: a Devil's staircase, Phys. Rev. Lett. 85 (2000) 3628–3631.
- [29] S.F. Edwards, The equations of stress in a granular material, Phys. A 249 (1998) 226–231
- [30] C.S. O'Hern, L.E. Silbert, A.J. Liu, S.R. Nagel, Jamming at zero temperature and zero applied stress: the epitome of disorder, Phys. Rev. E 68 (2003), 011306.
- [31] C.S. O'Hern, S.A. Langer, A.J. Liu, S.R. Nagel, Random packings of frictionless particles, Phys. Rev. Lett. 88 (2002), 075507.
- [32] L.E. Silbert, D. Ertaş, G.S. Grest, T.C. Halsey, D. Levine, Geometry of frictionless and frictional sphere packings, Phys. Rev. E 65 (2002), 031304.
- [33] M. van Hecke, Jamming of soft particles: geometry, mechanics, scaling and isostaticity, J. Phys. Condens. Matter 22 (2009), 033101.
- [34] V. Baranau, D. Hlushkou, S. Khirevich, U. Tallarek, Pore-size entropy of random hardsphere packings, Soft Matter 9 (2013) 3361–3372.
- [35] F. Göncü, O. Durán, S. Luding, Jamming in frictionless packings of spheres: determination of the critical volume fraction, 2009.

- [36] F. Göncü, O. Durán, S. Luding, Constitutive relations for the isotropic deformation of frictionless packings of polydisperse spheres, Comptes Rendus Mécanique 338 (2010) 570-586.
- N. Kumar, V. Magnanimo, S. Luding, Tuning the Bulk Properties of Bidisperse Granular Mixtures by Size Ratio, 2015.
- [38] N. Kumar, V. Magnanimo, M. Ramaioli, S. Luding, Tuning the bulk properties of bidisperse granular mixtures by small amount of fines, Powder Technol. 293 (2016) 94–112.
- [39] K. VanderWerf, W. Jin, M.D. Shattuck, C.S. O'Hern, Hypostatic jammed packings of frictionless nonspherical particles, Phys. Rev. E 97 (2018) 012909.
- [40] S.N. Coppersmith, C.h. Liu, S. Majumdar, O. Narayan, T.A. Witten, Model for force fluctuations in bead packs, Phys. Rev. E 53 (1996) 4673–4685.
- [41] T. Majmudar, M. Sperl, S. Luding, R.P. Behringer, Jamming transition in granular systems, Phys. Rev. Lett. 98 (2007), 058001.
- [42] M.L. Falk, J.S. Langer, Dynamics of viscoplastic deformation in amorphous solids, Phys. Rev. E 57 (1998) 7192–7205.
- (43) C.H. Rycroft, VORO++: a three-dimensional Voronoi cell library in C++, Chaos 19
- [44] A. Tordesillas, D.M. Walker, Q. Lin, Force cycles and force chains, Phys. Rev. E 81 (2010), 011302.
- [45] K. Mehlhorn, D. Michail, Minimum cycle bases: faster and simpler, ACM Trans. Algorithms 6 (2009) 1–13.
- [46] T.A. Harris, M.N. Kotzalas, Rolling Bearing Analysis, 5th ed. Taylor & Francis, Boca Raton, FL, 2006 ©2006.